buildings

MDPI

Article

Flexural Behavior of Fully Prefabricated Composite Bent Cap with Corrugated Steel Web

Zhiyu Cui [1], Panfeng Hou [2], Feiran Li [3,*], Wenru Lu [1] and Lu Huang [4]

[1] School of Civil Engineering, Henan University of Technology, Zhengzhou 450001, China; 15381427995@163.com (Z.C.); luwenru@haut.edu.cn (W.L.)
[2] Henan Transport Investment Group Co., Ltd., Zhengzhou 450016, China; 19063014392@163.com
[3] Henan Zhonggong Design & Research Group Co., Ltd., Zhengzhou 450003, China
[4] China Construction Seventh Engineering Division Corp., Ltd., Zhengzhou 450001, China; h15515633883@163.com
* Correspondence: 18539836692@163.com

Abstract

This study designed a novel fully prefabricated large-cantilevered composite bent cap with corrugated steel webs (CBC-CSW). Corrugated steel webs were employed to fully utilize the material properties of both steel and concrete, addressing the cracking issues prevalent in traditional concrete bent cap webs, achieving a self-weight reduction of over 50% and enabling fully prefabricated assembly construction. To investigate the flexural behavior, full-scale non-destructive static tests were conducted on two CBC-CSW specimens, and a finite element model was developed in ABAQUS and validated against experimental data. A parametric study was carried out to discuss the influence of key parameters. The results demonstrated that under the characteristic combination value for the serviceability limit state, all components remained elastic with excellent mechanical performance, and strain distributions complied with the plane section assumption, indicating a high safety margin. Flexural performance was enhanced by the steel flange, and flexural capacity could be increased by raising either the strength or the thickness of the flange. A formula for calculating the flexural capacity was proposed, with results closely matching experimental and finite element analysis data, demonstrating an error distribution within 5% to 7%.

Keywords: corrugated steel web; large-cantilevered composite bent cap; full-scale non-destructive static test; flexural behavior; numerical analysis

1. Introduction

In recent years, propelled by the advancement of China's strategy to become a global leader in transportation and the Belt and Road Initiative cooperation platform, prefabricated bridge technology, an integral component of modern industrialized bridge construction [1,2], is evolving into a key technology driving industry innovation. Prefabricated bridge technology in China has now matured, significantly enhancing construction efficiency and project quality in bridge engineering [3]. However, conventional concrete pier caps typically weigh between 200 and 600 tons [4] and are commonly constructed using cast-in-place methods, resulting in substantial on-site work, extensive labor requirements, and compromised construction efficiency [5]. While segmental precast pier caps improve construction efficiency [6–9], issues such as multi-stage prestressing operations and compromised structural integrity leading to web cracking persist, posing threats to durability and safety [4,10]. The fully prefabricated large-cantilever composite bent cap with corrugated

Check for updates

Academic Editor: Eric M. Lui

Received: 14 October 2026
Revised: 18 November 2026
Accepted: 23 November 2026
Published: 26 November 2026

Copyright: © 2026 by the authors. Licensee MDPI, Basel, Switzerland. This article is an open access article distributed under the terms and conditions of the Creative Commons Attribution (CC BY) license.

steel webs (CBC-CSW) is a structure replacing concrete webs with high-strength corrugated steel webs. This design fully utilizes the material properties of steel and concrete, effectively mitigating web cracking issues while significantly reducing the self-weight.

Corrugated steel webs were first applied in bridge engineering during the 1980s, when Dodin Campenon Bernard of France constructed the world's first composite bridge featuring this innovation—the Cognac Bridge [11]—based on model tests and theoretical analysis. This pioneering project has validated the technical superiority of corrugated steel webs in bridge structures [12–14]. Currently, over 400 bridges with corrugated steel web–concrete composite structures have been constructed worldwide [15,16]. In China, more than 160 such bridges have been built or are under construction [17], including the Juancheng Yellow River Bridge in Shandong, Xingtai Zijin Bridge, and Nanchang Chaoyang Bridge. With advancements in construction techniques and high-performance materials, these structures are increasingly evolving toward larger spans, wider decks, and fully prefabricated assembly [18–21].

Extensive research on conventional corrugated steel web composite beams has been conducted globally [11,22,23]. Existing studies have demonstrated that variations in corrugated steel web dimensions, flange plate properties, and material strength all affect the mechanical behavior of Composite bridge with corrugated steel webs [24–26]. Experiments by the Drexel team validated that webs in corrugated steel beams resist no bending moments [12]; Elamary et al. [27] investigated the effect of the top steel flange on the flexural behavior of corrugated steel webs, finding that its constraint effectively prevents web local buckling, enhancing structural stiffness and flexural capacity by nearly 30% and 12%, respectively; Bi et al. [28] proposed three evaluation metrics—the reduction coefficient, effective web width ratio, and additional flexural capacity ratio—to quantify the "accordion effect". They conducted a parametric analysis of steel strength, concrete strength, web height-to-width ratios, and flange-to-web thickness to investigate the effects of these factors on the flexural behavior of corrugated steel web structures; through experimental analysis of beams with corrugated steel webs, Metwally et al. [29] found that the bending contribution of corrugated steel webs was low due to their axial loading characteristics, with bending moments primarily borne by the reinforcement system. No significant interaction was observed between the flexural resistance of concrete and the shear resistance of corrugated steel webs. In developing computational methods, a mechanical response model for corrugated web I-beams was developed by Abbas et al. [23] based on nonlinear finite element numerical simulation. A quantitative analytical method for flange transverse bending strain was established, and its reliability was validated through comparative analysis of theoretical and experimental results; Oliveira et al. [30] developed a numerical model for continuous composite girders with sinusoidal corrugated steel webs, focusing on moment distribution characteristics and web deformation patterns in the elastic stage. Through parametric studies, they derived an analytical formula for the elastic critical moment and validated the reliability of this theoretical method using existing composite bridge data. In terms of innovative applications, a novel concrete-encased composite I-girder with corrugated steel webs was proposed by He et al. [31], whose flexural behavior and design methodology were investigated through experimental and theoretical analyses; Chen et al. [32] proposed a novel corrugated steel web composite box girder and investigated its flexural behavior through experimental tests and numerical simulations; He et al. [33] proposed a composite box girder incorporating corrugated steel webs and concrete-filled steel tubes. Its exceptional load-bearing capacity and ductility were demonstrated through full-scale tests. These findings demonstrate that composite bridges with corrugated steel webs have gained extensive global application owing to their advanced structural forms and load-bearing efficiency, establishing essential theoretical foundations for CBC-CSW flexural behavior research.

Furthermore, many researchers have adopted ABAQUS to conduct finite element simulations of corrugated steel web composite structures. Numerical models considering material nonlinearity, contact interaction and concrete damage plasticity were established to reproduce the load–deformation response, stress distribution and failure evolution of such members, and parametric analyses were further carried out to quantify the effects of web geometry, material strength and boundary conditions on structural performance [34]. These numerical studies provide effective tools for revealing the mechanical mechanism of corrugated steel web composite structures, while limited investigations focus on the full-precast bent caps with corrugated steel webs, which is the main research gap of the present work.

This paper experimentally and theoretically investigates the flexural behavior of CBC-CSW. Full-scale models of two CBC-CSW are fabricated based on the Zhengzhou–Xuchang section of the Zhengzhou–Nanyang Expressway project. Finite element models (FEM) established via ABAQUS 2021 software are employed to investigate the flexural behavior and failure mechanisms of the corrugated steel webs. Based on the plane section assumption, a calculation method for the flexural capacity of pier caps with corrugated steel webs is proposed. Its accuracy is verified by correlating experimental measurements with FEM, serving as a valuable reference for practical engineering applications of this novel bent cap.

2. Full-Scale Tests on CBC-CSW

2.1. Configuration of CBC-CSW

The CBC-CSW primarily comprises a concrete top plate, bottom plate, and corrugated steel webs, with its structural configuration as illustrated in Figure 1. Compared to traditional concrete bent cap, the CBC-CSW utilizes the strength advantages of high-strength steel. By transforming solid structures into thin-walled configurations with a high void ratio, it achieves over 50% self-weight reduction, enabling single-lift installation. With minimized prestressing tendons arrangements and factory completed tensioning, it significantly reduces on-site construction processes, fulfilling the requirements for fully prefabricated assembly.

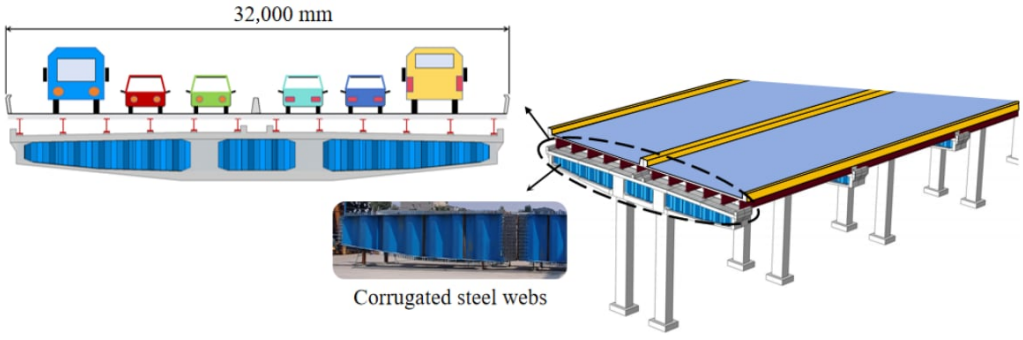

Figure 1. CBC-CSW.

2.2. Specimen Design

Two pieces of full-scale CBC-CSW specimens were designed and fabricated, designated as G-N4 and G-N5. Among them, at the precast yard, specimen G-N4 was tensioned with only prestressing tendons N1 to N4, while specimen G-N5 was tensioned with all tendons N1 to N5. The bent cap is subjected mainly to negative moments in the service stage, and all prestressing tendons are arranged in the top slab. Tendon N5 was not tensioned in G-N4 mainly because tensioning all tendons simultaneously under self-weight could easily induce cracking in the bottom slab; however, deferring tendon N5 to elevated tensioning after the

pier was erected would increase the difficulty of high-altitude work and be unfavorable to prefabricated construction. Prior to formal loading, specimen G-N5 was fabricated in parallel, with all its prestressing tendons tensioned at the precast yard, and bottom-slab crack monitoring was conducted during tensioning to verify that this corrugated steel web bent cap can achieve integral tensioning at the precast yard. The two specimens were otherwise identical in geometry and material configuration. The test specimen features a 3.1 m height from the top plate surface to the bottom plate surface of concrete, with a 2.6 m width at the top plate and a 2.4 m width at the bottom plate. The point of vertical intersection of the top and bottom plate are both positioned 4.9 m from the centerline of the full section, while the cross slope on both sides of the top plate is 2%. Detailed dimensions are shown in Figure 2a,b illustrates the schematic configuration of the CBC-CSW. These webs are fabricated by welding corrugated steel plates with thicknesses t of 12 mm, 16 mm, 18 mm, and 20 mm. The upper flange and lower flanges employ steel plates of 16 mm and 20 mm thickness, respectively. Along the longitudinal direction of the bent cap, the straight web panel measures 430 mm in length, while the inclined panel extends 370 mm, yielding a wavelength of 800 mm and a wave height of 220 mm. The arrangement of prestressing tendons in the concrete top plate is depicted in Figure 2c.

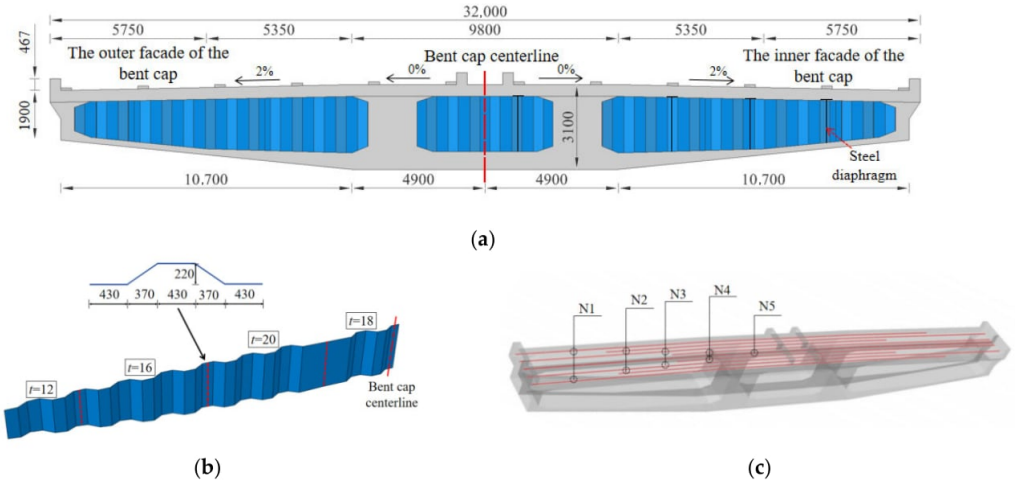

Figure 2. The overall structure of CBC-CSW and the details of its components: (**a**) the overall structure of CBC-CSW (unit: mm); (**b**) schematic diagram of corrugated steel webs; (**c**) layout plan of prestressing tendons in top plate of CBC-CSW.

2.3. Material

The CBC-CSW were cast with C60-grade concrete. The corrugated steel webs were fabricated from Q420D low-alloy high-strength structural steel, while common steel rebars consisted of hot-rolled ribbed bars (HRB400). Prestressing tendons were composed of 1 × 17 Φ15.24 prestressing steel bundles with a characteristic tensile strength f_{pk} of 1860 MPa. The material properties are summarized in Table 1.

Table 1. Material properties of CBC-CSW.

Material	f_{cu} (MPa)	f_y (MPa)	f_{ck} (MPa)	ν	E (GPa)
C60	62.1	—	40.9	0.2	36.2
HRB400	—	410.2	—	0.3	201.4
Q420D	—	420.0	—	0.3	206.0

2.4. Loading Program

The CBC-CSW specimens were fabricated in the prefabrication yard and then transferred to the test platform, with rubber bearings installed between the bent caps and the test platform. A reaction frame system was designed for the test. The reaction frame was constructed by welding I-beams, with a total steel consumption of 57 tons for a single frame. A counterweight area was arranged on the reaction frame, utilizing readily available ordinary rebars from the prefabrication yard as counterweights, as shown in Figure 3. The formal vertical loads were applied using eight jacks jointly controlled by four oil pumps, with the maximum load set to the characteristic combination value for the serviceability limit state. The test loading was divided into two stages: preloading and formal loading. The preload value was set at 10% of the maximum load. The formal loading was conducted in ten stages: stages 1–5 constituted the loading process, with stage 5 reaching the maximum test load. Four independent loading points, designated Q1, Q2, Q3, and Q4, were arranged at each end of the bent cap; the maximum applied load at each individual loading point Q1–Q4 was 2252.0 kN, 1284.6 kN, 1284.6 kN, and 1323.3 kN, respectively. Stages 6–10 comprised the corresponding unloading process.

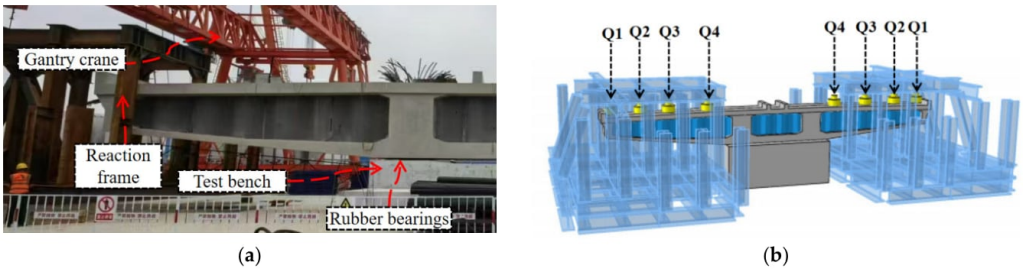

Figure 3. The experiment loads the general layout: (**a**) experimental loading layout; (**b**) the experiment loads the simulated layout drawing.

2.5. Test Setup

Along the bent cap length, five concrete sections (1-1 to 5-5) and three corrugated steel web sections (a-a to c-c) were arranged. Strain gauges were mounted on the top and bottom plates, while strain rosettes were deployed on the corrugated steel webs. Additionally, a cantilever truss beam was embedded in the test platform, with five displacement sensors arranged along its length to measure vertical displacement of the bent cap. This configuration effectively eliminates displacement variations induced by foundation settlement. Specifically, transducer F5 was positioned adjacent to the rubber bearing to capture its elastic compression. The sensor layout on the specimen is illustrated in Figures 4 and 5.

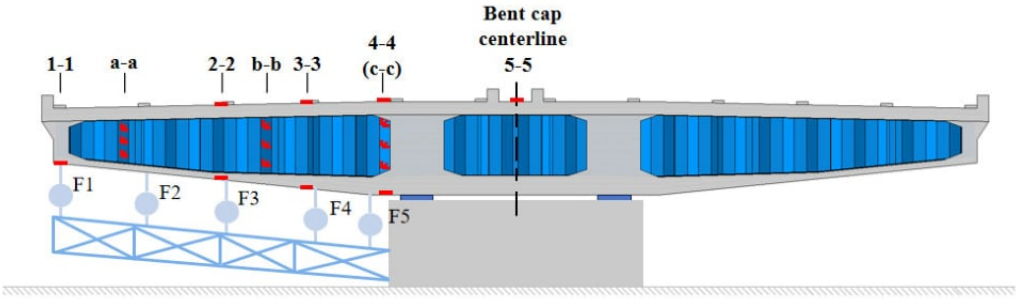

Figure 4. Schematic of instrumentation arranged for vertical deflection measurement on CBC-CSW.

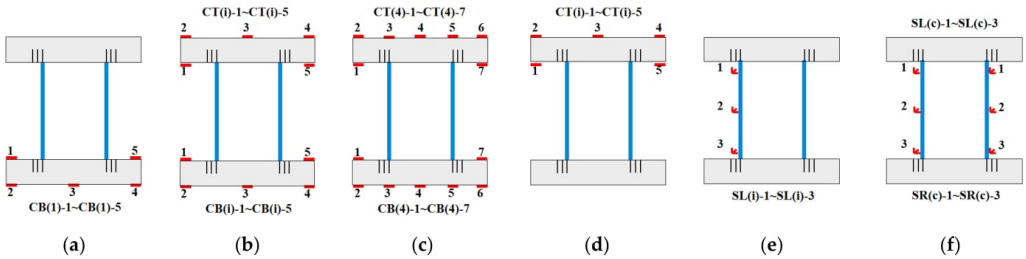

Figure 5. Cross-sectional arranged of the bent cap: (**a**) 1-1 section; (**b**) 2-2 and 3-3 section; (**c**) 4-4 section; (**d**) 5-5 section; (**e**) a-a and b-b section; (**f**) c-c section.

2.6. Experimental Results and Discussion

2.6.1. Experimental Load–Displacement Curves

Figure 6 demonstrates the mechanical response characteristics of the specimens. During the initial loading stage, a proportional relationship exists between the applied load and displacement at each section. When the load reaches the characteristic combination value for the serviceability limit state (Level 5), the maximum deflections of G-N4 and G-N5 are 17.22 mm and 24.69 mm, respectively, both occurring at Section 1-1. This may be attributed to geometric nonlinearity induced by the larger initial upward camber of G-N5, resulting in a greater reduction in its camber under loading. The structural stiffness remains essentially constant, and no cracks appear on the specimen surfaces. After completing unloading (Stage 10), the deflection values at all cross-sections return to virtually zero, with no visible cracks forming on the specimen surface. This confirms that the CBC-CSW remained within the elastic working stage throughout the testing process.

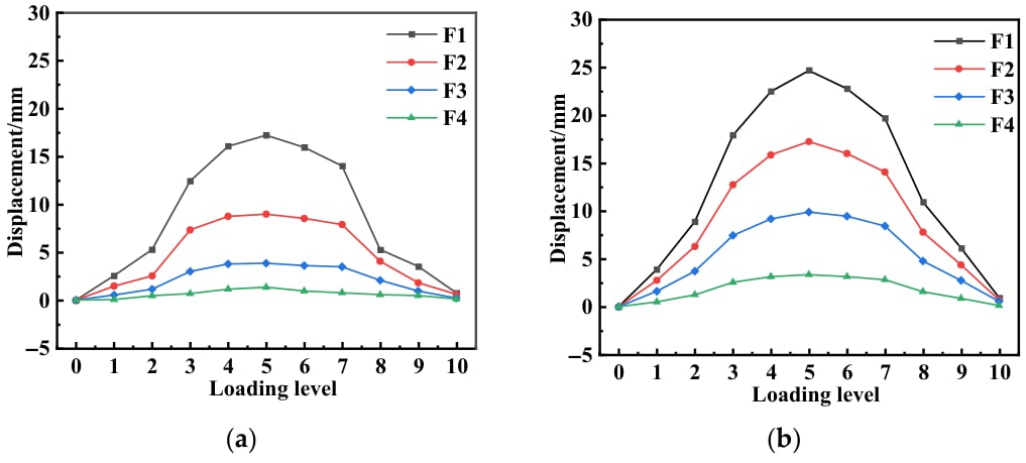

Figure 6. Load–displacement curves of CBC-CSW: (**a**) G-N4; (**b**) G-N5.

2.6.2. Concrete Strain

The load–strain curves recorded at midspan measuring points of both the top and bottom plate in the CBC-CSW are shown in Figures 7 and 8, respectively. Figures 7 and 8 indicates that during loading, the concrete top plate is primarily subjected to tension, while the bottom plate is dominated by compression. When the load reaches the characteristic combination value for the serviceability limit state (Level 5), the maximum tensile stresses of the top plate of G-N4 and G-N5 are 15.45 MPa and 16.18 MPa, respectively. The maximum tensile stress occurs at the bent cap centerline (Section 5-5), and the maximum compressive stress of the bottom plate appears at the root of the cantilever segment (Section 4-4), with values of −11.75 MPa for G-N4 and −9.02 MPa for G-N5. The stress is calculated by multiplying the measured strain by the elastic modulus of concrete. Since the initial readings

were collected after the pre-tensioning of all prefabricated components in this test, the reported stresses are only the stress increments generated during loading and exclude the pre-compressive stress induced by prestress. Following completion of unloading (Level 10), the residual tensile strains at all measurement points of the CBC-CSW approach zero, with no points exhibiting plastic tendencies. This observation indicates that both the top and bottom concrete plate remain in an elastic working stage throughout the entire test process.

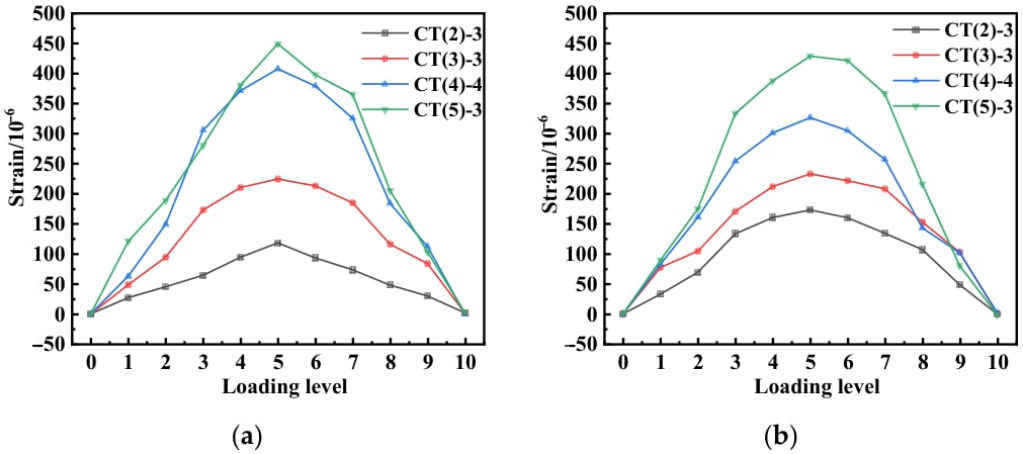

Figure 7. Load–strain curve of top plate in CBC-CSW specimen: (**a**) top plate of G-N4; (**b**) top plate of G-N5.

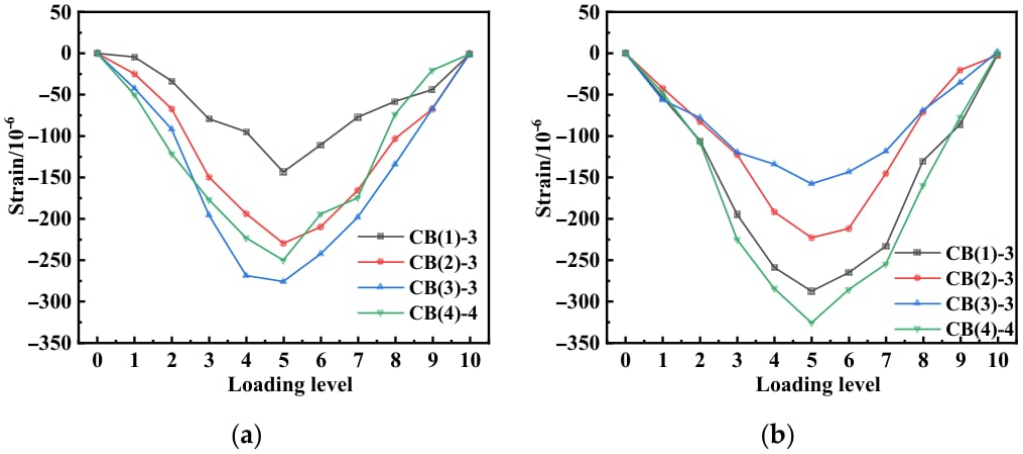

Figure 8. Load–strain curve of bottom plate in CBC-CSW specimen: (**a**) bottom plate of G-N4; (**b**) bottom plate of G-N5.

2.6.3. Corrugated Steel Web Strain

The load–strain curves for corrugated steel webs at various sections of specimens G-N4 and G-N5 are presented in Figures 9 and 10, respectively. For specimen G-N4, when the load reaches the characteristic combination value for the serviceability limit state (Level 5), the maximum tensile stress of 36.33 MPa appears at the b-b section of the corrugated steel web, while the maximum compressive stress of −71.28 MPa occurs at the a-a section. For specimen G-N5, the strain distribution pattern is similar, with a maximum tensile stress of 32.76 MPa and a maximum compressive stress of −65.41 MPa under the same load level. After unloading completion (Level 10), all residual tensile strains at measurement points of the corrugated steel webs of both specimens approach zero, with no gauges exhibiting plastic deformation. This observation demonstrates that the corrugated steel webs of both specimens remain in the elastic working stage throughout the entire test.

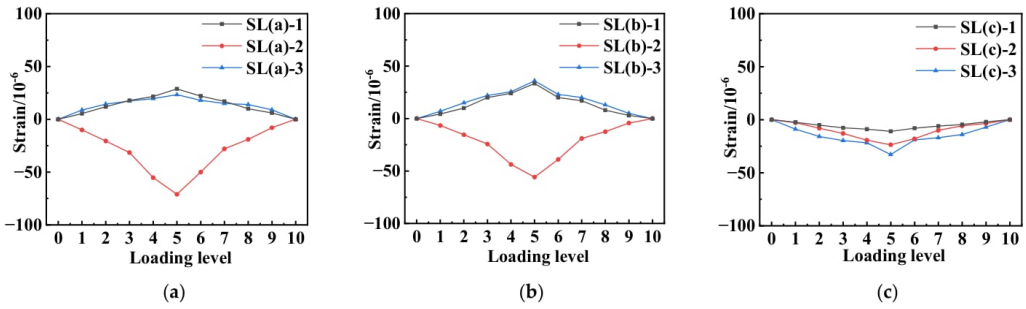

Figure 9. Longitudinal strain distribution of corrugated steel webs for specimen G-N4: (**a**) a-a section; (**b**) b-b section; (**c**) c-c section.

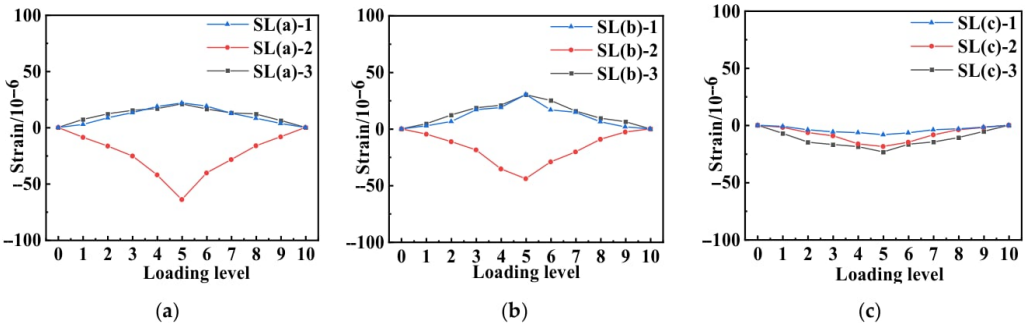

Figure 10. Longitudinal strain distribution of corrugated steel webs for specimen G-N5: (**a**) a-a section; (**b**) b-b section; (**c**) c-c section.

2.6.4. Distribution of Strain Through the Height in CBC-CSW

Figure 11 presents the measured strain distributions along the height of the web in section 4-4 of the G-N5 specimen under various loading conditions. It is observed that strain distributions maintain a predominantly linear pattern along the beam height under all load levels. Since the flexural strength of specimens is predominantly provided by the top plate and flanges, the webs contribute negligibly when loaded to the characteristic combination value for the serviceability limit state. This confirms that the strain distribution across the test beam sections complies with the plane section assumption [35].

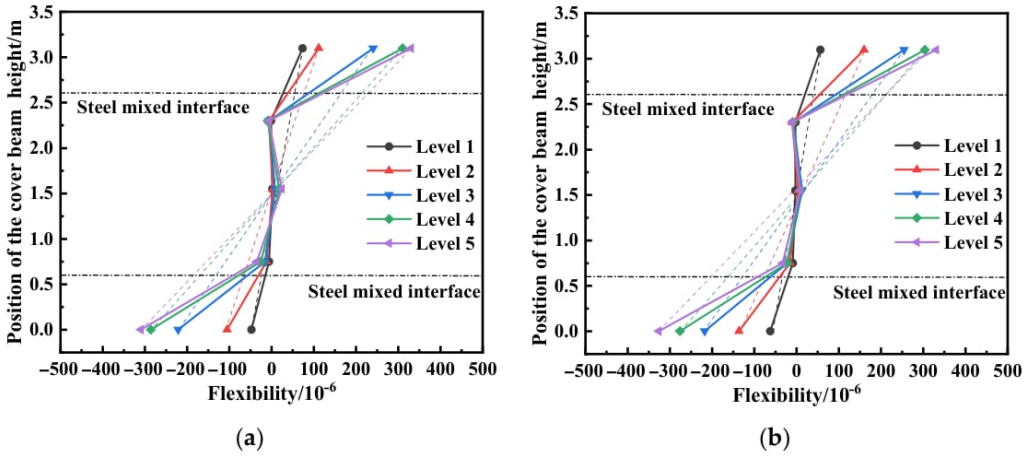

Figure 11. G-N5 strain distribution along the height direction: (**a**) L side of 4-4 cross-section; (**b**) R side of 4-4 cross-section.

3. Finite Element Model

3.1. Model Building

A finite element model (FEM) of the G-N5 CBC-CSW was developed using ABAQUS 2021 software. The FEM of the CBC-CSW and the mesh division of its components are illustrated in Figure 12. Concrete and loading pads were modeled with C3D8R reduced-integration solid elements, which offer high computational efficiency and effectively alleviate shear locking, with a target element size of 180 mm. The corrugated steel plates and steel diaphragms were modeled with S4R shell elements, which are suitable for representing thin-plate behavior and balance computational accuracy and efficiency, with a target element size of 160 mm. The prestressing tendons and common steel rebars were modeled with T3D2 truss elements, which carry only axial tensile forces [34]. Structured meshing was adopted in regions with regular geometry, while mapped meshing was used in locally irregular regions such as chamfers; the mesh scheme was determined through a mesh convergence study. The prestressing force was applied by the cooling-down method, in which a predefined temperature field was used to simulate the pre-compressive stress developed in the concrete after the prestressing tendons were tensioned. The binding constraints were applied at the interface between the concrete top and bottom plate and corrugated steel webs, while steel diaphragms, corrugated steel webs, upper flanges, and lower flanges were merged by sharing nodes. Two constraint points were set between the corrugated steel web bent cap model and the loading frame to simulate the simply supported boundary conditions: one point was constrained in ($U_X = U_Y = U_Z = U_{RZ} = 0$), and the other in ($U_X = U_Y = U_{RY} = U_{RZ} = 0$).

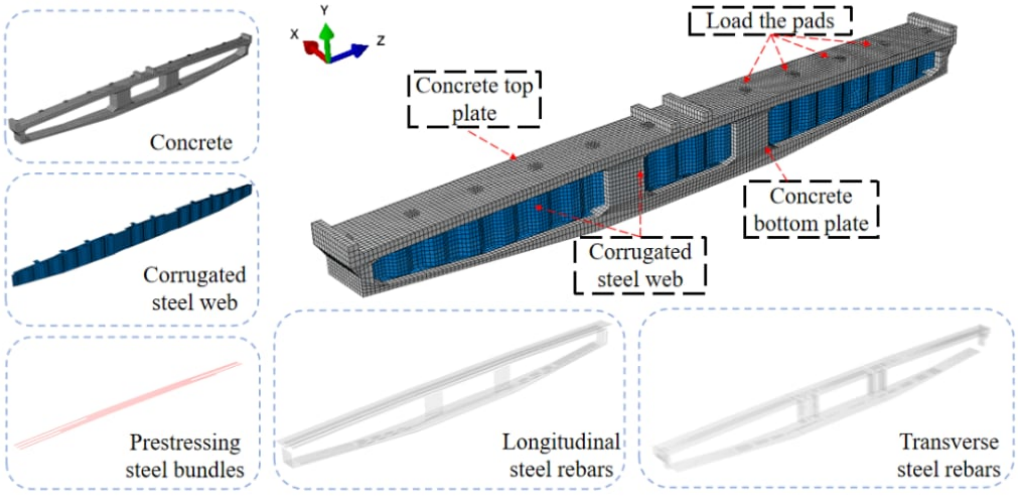

Figure 12. FEM of CBC-CSW.

3.2. Material Constitutive Models

The Concrete Damage Plasticity (CDP) model in ABAQUS was adopted to simulate concrete behavior, with its tensile and compressive stress–strain curves determined according to the Standard for Design of Concrete Structures (GB 50010-2010) [36]; The corresponding CDP parameters are summarized in Table 2, and the uniaxial tensile and compressive damage evolution laws are given in Equations (1) and (2); The corrugated steel webs were modeled using a three-segment elasto-plastic constitutive model [37]; The prestressing tendons were modeled with a two-segment polyline approach [38]; The common steel rebars was modeled with an ideal elastoplastic constitutive model [39], and its stress–strain behavior is illustrated in Figure 13.

$$d_t = \begin{cases} 1 - \frac{f_{t,r}}{E_c \varepsilon_{t,r}} \left[1.2 - 0.2 \left(\frac{\varepsilon}{\varepsilon_{t,r}} \right)^5 \right], & \varepsilon \le \varepsilon_{t,r} \\ 1 - \frac{f_{t,r}}{E_c \varepsilon_{t,r}} / \left[\alpha_t \left(\frac{\varepsilon}{\varepsilon_{t,r}} - 1 \right)^{1.7} + \frac{\varepsilon}{\varepsilon_{t,r}} \right], & \varepsilon > \varepsilon_{t,r} \end{cases} \quad (1)$$

where ε is the uniaxial tensile strain of concrete; E_c is the elastic modulus of concrete (MPa); α_t is the parameter of the descending branch of the uniaxial tensile stress–strain curve, taken as 2.515; $f_{t,r}$ is the uniaxial tensile strength (MPa), taken as 2.84; $\varepsilon_{t,r}$ is the peak tensile strain corresponding to $f_{t,r}$, taken as 1.0×10^{-4}; d_t is the tensile damage evolution parameter.

$$d_c = \begin{cases} 1 - \frac{f_{c,r}}{f_{c,r} + (E_c \varepsilon_{c,r} - f_{c,r}) \left(\frac{\varepsilon}{\varepsilon_{c,r}} \right)^{\frac{E_c \varepsilon_{c,r}}{E_c \varepsilon_{c,r} - f_{c,r}}}}, & \varepsilon \le \varepsilon_{c,r} \\ 1 - \frac{f_{c,r}}{E_c \varepsilon_{c,r}} / \left[\alpha_c \left(\frac{\varepsilon}{\varepsilon_{c,r}} - 1 \right)^2 + \frac{\varepsilon}{\varepsilon_{c,r}} \right], & \varepsilon > \varepsilon_{c,r} \end{cases} \quad (2)$$

where ε is the uniaxial compressive strain of concrete; E_c is the elastic modulus of concrete (MPa); α_c is the parameter of the descending branch of the uniaxial compressive stress–strain curve, taken as 1.86; $f_{c,r}$ is the uniaxial compressive strength (MPa), taken as 38.5; $\varepsilon_{c,r}$ is the peak compressive strain corresponding to $f_{c,r}$, taken as 1.7×10^{-3}; d_c is the compressive damage evolution parameter.

Table 2. Parameters of the concrete damaged plasticity (CDP) model.

Dilation Angle, ψ (°)	Eccentricity, e	f_{b0}/f_{c0}	Stress Ratio, K_c	Viscosity Parameter, μ
30°	0.1	1.16	0.66667	0.00075

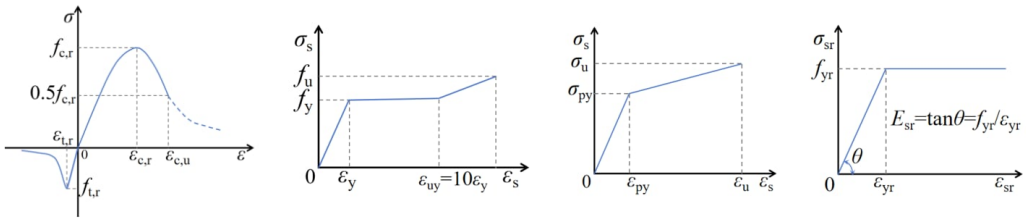

Figure 13. Material constitutive curves: (**a**) concrete; (**b**) corrugated steel webs; (**c**) prestressing tendons; (**d**) common steel rebars.

The material constitutive models used in the finite element simulation are illustrated in Figure 13. For concrete (Figure 13a), the uniaxial tensile and compressive stress–strain curves are described by the CDP model given in Equations (1) and (2). For the corrugated steel webs (Figure 13b), a three-stage elasto-plastic model is adopted, with the yield strength f_y = 420 MPa and the ultimate strength $f_u = 1.2 f_y$ = 504 MPa. For the prestressing tendons (Figure 13c), a bilinear model is used, with the nominal yield strength σ_{py} = 1395 MPa and the ultimate strength σ_u = 1860 MPa. For the common steel rebars (Figure 13d), an ideal elasto-plastic model is employed, with the yield strength f_{yr} = 410.2 MPa and the elastic modulus E_{sr} = 201.4 GPa.

3.3. Finite Element Results Verification

3.3.1. Load–Displacement Curves

A comparison between the FEM and test load–displacement curves is presented in Figure 14. As shown in Figure 14, the load–displacement curves from finite element simulation and experimental testing are compared. The maximum deflection discrepancy between the simulated and measured values is less than 2 mm, with a relative error below 10%. The

deflection ratio predominantly ranges from 0.85 to 1.15, yielding a mean absolute error of 15%. These results demonstrate high precision of the FEM in simulating the deflection response of CBC-CSW.

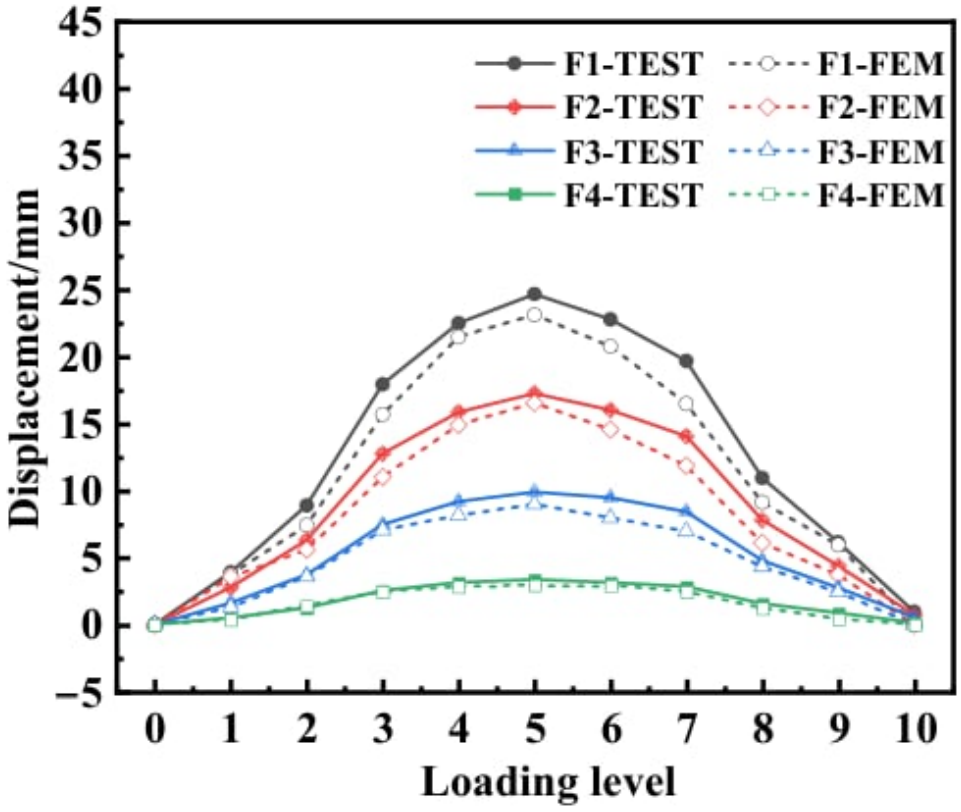

Figure 14. Comparison of the test with the FEM load–displacement curve.

3.3.2. Load-Strain Curves

The comparison between FEM and test load–strain curves is illustrated in Figure 15. Relative errors between the maximum strains of the FEM and the test are 0.5% and 10.9% for the concrete top and bottom plate, respectively, and 3% and 6.2% for the corrugated steel webs across sections, respectively. After unloading, the FEM exhibits no residual strain, which aligns with test results, while the relative error between FEM and test strains remains below 15%. These results demonstrate the high accuracy of the FEM in simulating strain responses.

3.4. The Failure Process of CBC-CSW

3.4.1. Forms of Destruction

The finite element simulation employed a five-stage loading–unloading scheme based on the actual test conditions, with both the load amplitude and loading history calibrated against the target values from the test. During the initial loading phase, when the load reached the characteristic combination value for the serviceability limit state, the CBC-CSW exhibited no damage; the deformations of both the corrugated steel webs and the prestressing tendons remained at an extremely low level, and the concrete as a whole maintained a linear elastic working state.

As the load increased further, when the load reached 23,146.4 kN, initial tensile cracks first appeared in concrete Section 4-4 at the cantilever root of the top slab. After the top-slab concrete cracked in tension, the cracked concrete ceased to resist bending moment, and the

bending moment at this section was resisted jointly by the prestressing tendons, ordinary steel rebars, and the steel flange of the top slab.

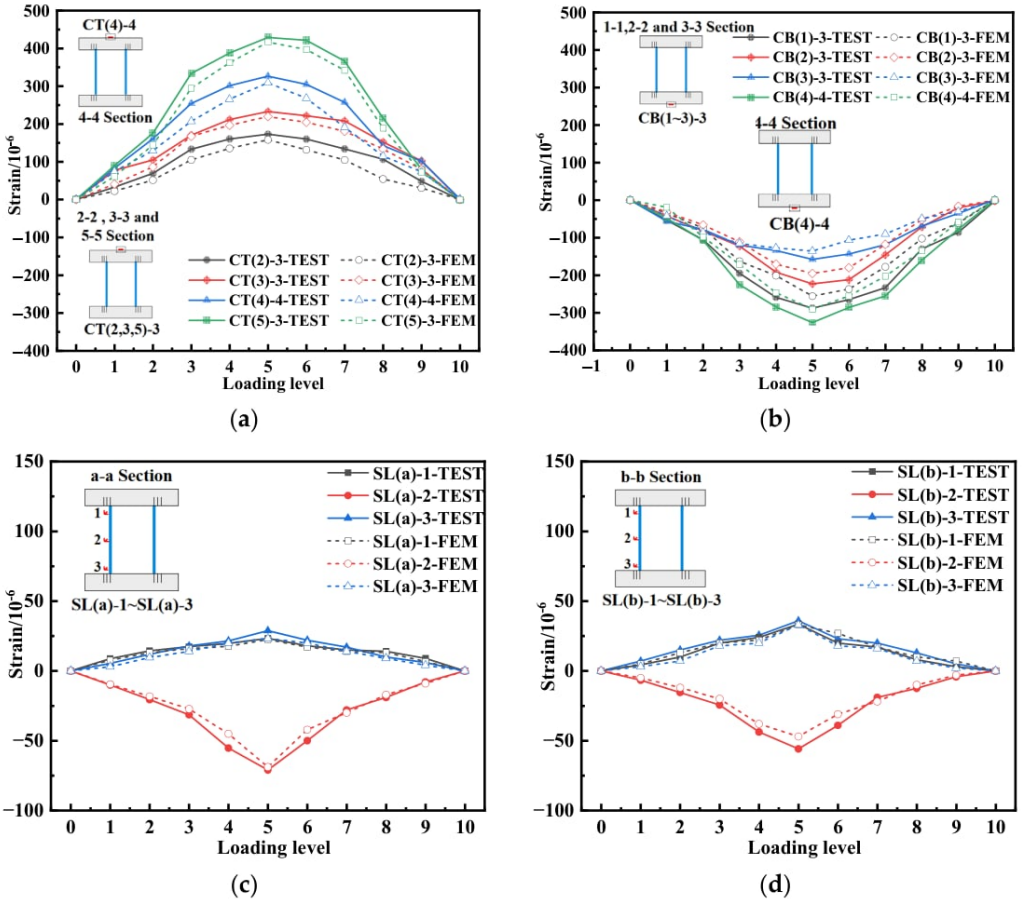

Figure 15. Comparison of the test with the FEM load-strain curve: (**a**) top plate; (**b**) bottom plate; (**c**) a-a section; (**d**) b-b section.

When the load further increased to 34,275.7 kN, the bent cap reached its ultimate bearing capacity and failed. At this stage, cracks developed most severely in the top slab near the bent cap centerline and at the cantilever root section, while the bottom-slab concrete at the cantilever root underwent crushing failure; the high-stress regions in the corrugated steel webs were concentrated mainly around the cantilever root of the bent cap. Based on the observed crack development and stress distribution characteristics, the CBC-CSW exhibited a typical flexural failure mode. Table 3 presents the progressive development of concrete cracks and the stress evolution of each steel component throughout the entire loading process. Specifically, DAMAGEC and DAMAGET denote the compressive and tensile damage variables of the concrete damaged plasticity model, respectively, ranging from 0 to 1; a value closer to 1 indicates a higher degree of damage in the corresponding regime. The von Mises equivalent stress is used primarily to assess the yield state of steel components under multiaxial stress. S11 denotes the normal stress along the longitudinal direction of the bent cap, reflecting the tensile or compressive stress level of the member in the longitudinal direction.

Table 3. Failure process of concrete roof/bottom plate and steel components in CBC-CSW.

Specimen	Characteristic Combination Value for the Serviceability Limit State	Initial Crack State of Concrete	Achieve the Ultimate Bearing Capacity
Concrete top plate	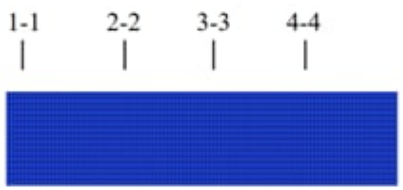	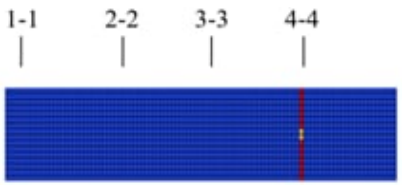	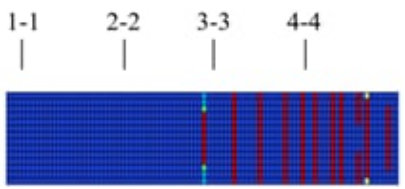
Concrete bottom plate			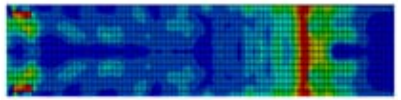
Corrugated steel web			
Prestressing tendons		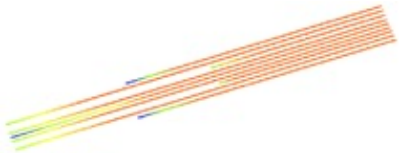	

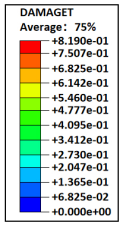

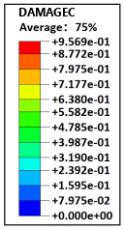

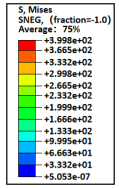

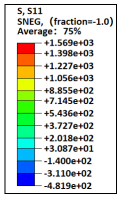

3.4.2. Load–Displacement Curves

The load–displacement curve of the CBC-CSW throughout the loading process is shown in Figure 16, where Pu (34,275.7 kN) denotes the ultimate bearing capacity. As indicated by the curve, the loading process can be divided into three distinct stages. Stage I (Elastic Stage): Until the load reaches 0.68 Pu, the deflection of the CBC-CSW increases linearly with increasing load, as expected. Stage II (Yielding Phase): When the load attains 0.68 Pu, the deflection of the CBC-CSW increases nonlinearly. As the load progresses, deflections at all sections progressively intensify. Stage III (Failure Phase): When the load reached 0.94 Pu, a marked increase in deflection was observed. Structural failure occurred at the ultimate load (Pu).

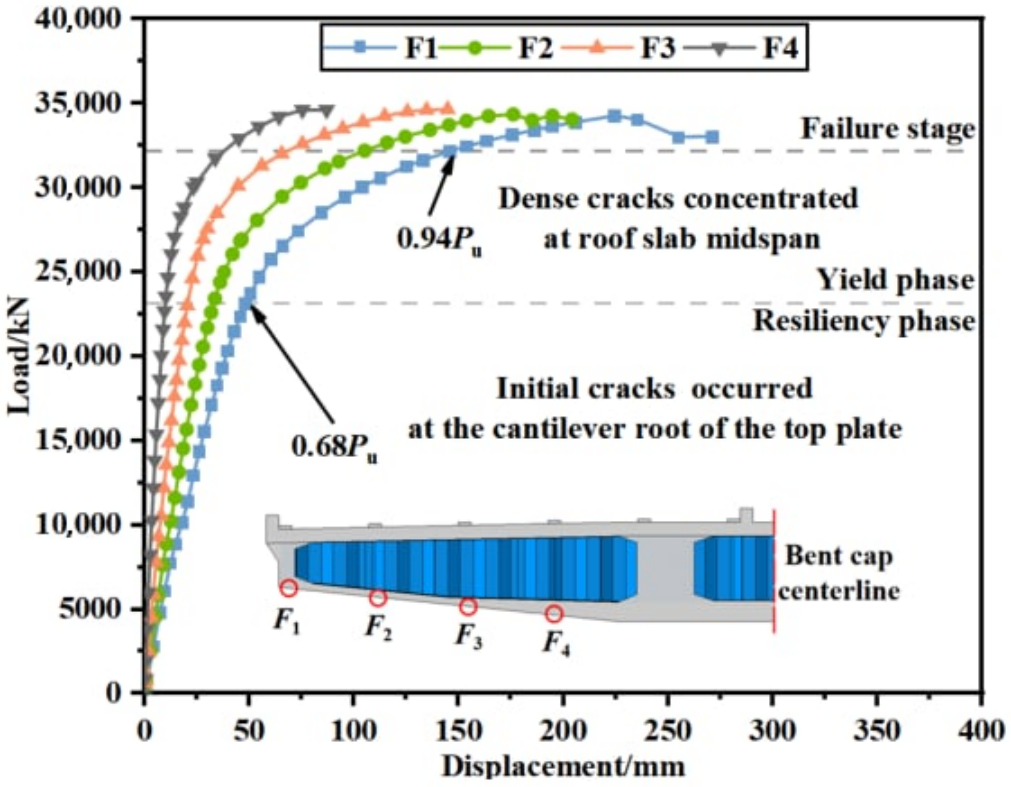

Figure 16. Load–displacement curve of CBC-CSW during failure.

4. Parameter Sensitivity Analysis

Based on the validated FEM established previously, ultimate bearing capacity analysis of the CBC-CSW was conducted by systematically varying the concrete strength, steel strength, corrugated steel web thickness, and flange plate thickness. All other parameters remain unchanged throughout the parametric study.

4.1. Effect of the Concrete Strength

Figure 17a illustrates the ultimate bearing capacity of the CBC-CSW under varying concrete strengths. When the concrete strength was increased from 50 MPa to 60 MPa, 70 MPa, and 80 MPa, the CBC-CSW exhibited flexural failure, with their flexural capacity increasing by 4.45%, 3.89%, and 4.56%, respectively. It is evident that concrete strength exerts a limited influence on the ultimate bearing capacity of CBC-CSW. Beyond a certain grade, no significant increase in ultimate bearing capacity is observed.

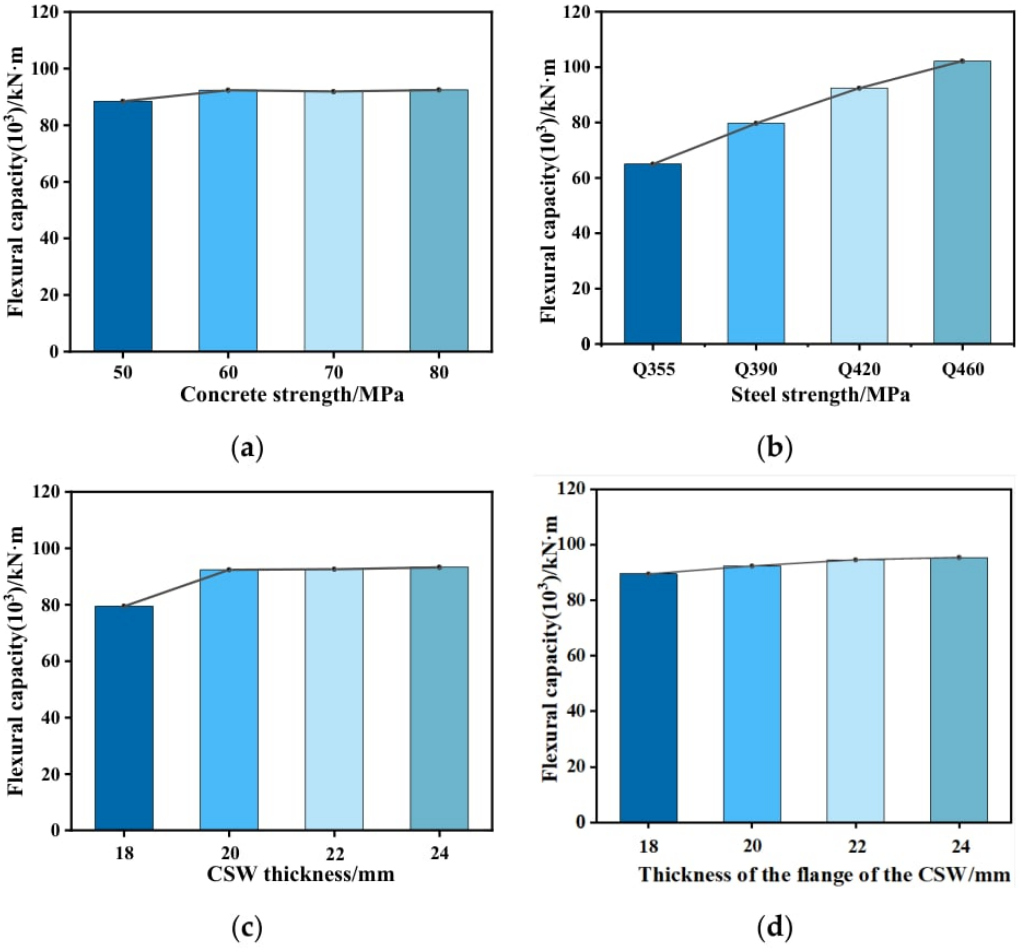

Figure 17. Effect of different parameters on ultimate bearing capacity: (**a**) effect of concrete strength on ultimate bearing capacity; (**b**) effect of steel strength on ultimate bearing capacity; (**c**) effect of corrugated steel web thickness on ultimate bearing capacity; (**d**) effect of thickness of the flange of the corrugated steel web on ultimate bearing capacity.

4.2. Effect of the Strength of the Steel

The ultimate bearing capacity of CBC-CSW under varying steel strengths are demonstrated in Figure 17b. As shown in Figure 17b, the variation in steel strength significantly influences the ultimate bearing capacity. When the steel strength was increased from 355 MPa to 390 MPa, 420 MPa, and 490 MPa, the ultimate bearing capacity increased by 22.71%, 42.21%, and 57.25%, respectively. This is attributed to the fact that changes in steel strength altered the failure modes of the bent cap. At steel strengths of 355 MPa and 390 MPa, shear failure occurred in the corrugated steel webs at the cantilever root. In contrast, at steel strengths of 420 MPa and 490 MPa, the failure mode shifted to flexural failure. Furthermore, since the corrugated steel webs and their flanges were made of the same steel material, the steel flanges could work in concert with the concrete top plate to resist the bending moment. Consequently, when the steel strength was raised from 420 MPa to 490 MPa, the ultimate bearing capacity of the bent cap saw a further increase of 15.04%.

4.3. Effect of the Corrugated Steel Web Thickness

The ultimate bearing capacity of CBC-CSW under varying corrugated steel web thicknesses is illustrated in Figure 17c. As a corrugated steel web thickness of 18 mm, the bent cap failed due to shear in the webs at the cantilever root. In contrast, under load, the bent caps with web thicknesses of 20 mm, 22 mm, and 24 mm all exhibited flexural failure.

Compared to the specimen with an 18 mm web thickness, their ultimate bearing capacities increased by 16.25%, 16.52%, and 17.35%, respectively.

4.4. Effect of the Corrugated Steel Web Flange Thickness

The ultimate bearing capacity of the CBC-CSW under different flange thicknesses is illustrated in Figure 17d. As observed, the ultimate bearing capacity remains relatively stable with increasing flange thickness. When the flange thickness rises from 18 mm to 20 mm, 22 mm, and 24 mm, the ultimate bearing capacity increases by 3.26%, 5.73%, and 6.69%, respectively. Flexural failure was observed in all the CBC-CSW under loading. Compared with steel strength and corrugated steel web thickness, the flange thickness exerts a lesser influence on the ultimate bearing capacity.

5. Calculation Formula for the Flexural Capacity of CBC-CSW

5.1. Mechanical Model of CBC-CSW

The corrugated steel webs in the CBC-CSW are transformed into flat steel plates through the equivalent method theory, with one complete wavelength segment analyzed and its dimensional parameters illustrated in Figure 18. A pair of axial forces F_N is applied to the corrugated steel web and equivalent flat steel plate, respectively, with the web height of the equivalent flat steel plate at a distance x from the short edge denoted as $h(x)$.

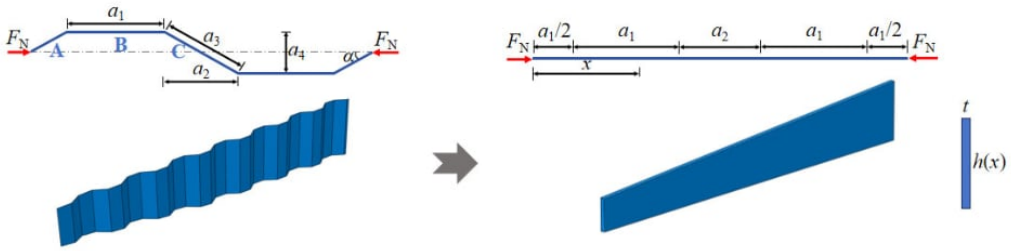

Figure 18. Individual band dimensions.

The axial deformation of an individual corrugation panel in a corrugated steel web, denoted as δ_{SW}, is calculated:

$$\begin{aligned}\delta_{SW} &= 2\left[\int_0^{\frac{a_3}{2}} \frac{M_A\overline{M_A}}{E_sI}dx_1 + \int_0^{a_1} \frac{M_B\overline{M_B}}{E_sI}dx_2 + \int_0^{\frac{a_3}{2}} \frac{M_C\overline{M_C}}{E_sI}dx_3\right] \\ &= \frac{2F_N}{E_sht^3}(a_3a_4{}^2 + 3a_1a_4{}^2)\end{aligned} \tag{3}$$

where E_s is defined as the elastic modulus of the corrugated steel web, M_A, M_B and M_C denote the bending moment values within sections A to C.

The cross-sectional area of the equivalent flat steel plate varies linearly along its length, with the area $A(x)$ at a distance x from the short edge given by:

$$A(x) = t \cdot \left[h_1 + \frac{(h_2 - h_1)}{L} \cdot x\right] \tag{4}$$

where h_1 is defined as the equivalent flat steel plate height at the tip of the cantilever segment, and h_2 represents the equivalent flat steel plate height at the root section of the cantilever segment.

By integrating the axial deformation over its differential segment d_x, the axial deformation δ_{eq} for an individual corrugation unit is expressed as:

$$\delta_{eq} = \int_0^L \frac{F_N}{E_{eq} \cdot A(x)} dx \tag{5}$$

where E_{eq} is defined as the equivalent elastic modulus of steel plate, L denotes the design length of the equivalent plate.

Substituting L and A(x) into Equation (5) yields:

$$\delta_{eq} = \frac{F_N}{E_{eq} \cdot t} \cdot \frac{a_1 + a_2}{h_2 - h_1} \cdot \ln\left(\frac{h_2}{h_1}\right) \tag{6}$$

To achieve identical deformation between the corrugated steel web and the equivalent flat steel plate under axial force F_N, the ratio Γ of the axial elastic modulus of the equivalent flat steel plate to that of the corrugated steel web is expressed as:

$$\Gamma = \frac{E_{eq}}{E_s} = \frac{(a_1 + a_2)ht^2}{2(h_2 - h_1)(a_3a_4^2 + 3a_1a_4^2)} \cdot \ln\left(\frac{h_2}{h_1}\right) \tag{7}$$

By calculation the elastic modulus ratio between corrugated steel webs and their equivalent flat steel plates, with the results presented in Table 4. It can be observed that the "accordion effect" significantly reduces the axial elastic modulus of corrugated steel web pier caps. The ratio of axial stiffness elastic modulus between corrugated steel webs and corresponding flat steel plates is less than 1%. Moreover, the thinner the web thickness, the more pronounced the accordion effect and the greater the reduction amplitude in axial elastic modulus.

Table 4. Comparison of the elastic modulus of corrugated steel web and equivalent flat steel plate.

Contrast Positions	a_1 (mm)	a_2 (mm)	a_3 (mm)	a_4 (mm)	t (mm)	h (mm)	h_1 (mm)	h_2 (mm)	E_{eq}/E_s
h_1	430	370	430	220	20	2003	2003	2030	0.0075 (Γ1)
h_2	430	370	430	220	20	2030	2003	2030	0.0082 (Γ2)
h_1	430	370	430	220	12	1198	1198	1338	0.0028 (Γ3)
h_2	430	370	430	220	12	1338	1198	1338	0.0031 (Γ4)

5.2. Analysis of Flexural Behavior of CBC-CSW

A half model of the CBC-CSW is adopted to analyze its mechanical behavior. Under the assumed external load conditions illustrated in Figure 19, symmetrical loads F_1–F_4 are applied at the loading blocks on the cantilever segment. The y-y cross-section at the cantilever root is selected as the representative section for structural ultimate failure. Concentrated loads F_1–F_4 are applied at distances x_1, x_2, x_3 and x_4 from this section, with boundary constraints existing at the supports and the pier cap centerline. The bending moment borne by the y-y section is the superposition of moments generated by external loads F_1–F_4.

The bending moment about the y-y axis of the CBC-CSW is denoted as M_y, calculated as follows:

$$M_y = x_1F_1 + x_2F_2 + x_3F_3 + x_4F_4 \tag{8}$$

The reinforcement configuration at the y-y section is illustrated in Figure 20a. The neutral axis location of the corrugated steel web is determined based on the force equilibrium conditions of concrete, reinforcement, and steel flange in the cross-section, thereby delineating the tension and compression zones, presented in Figure 20b.

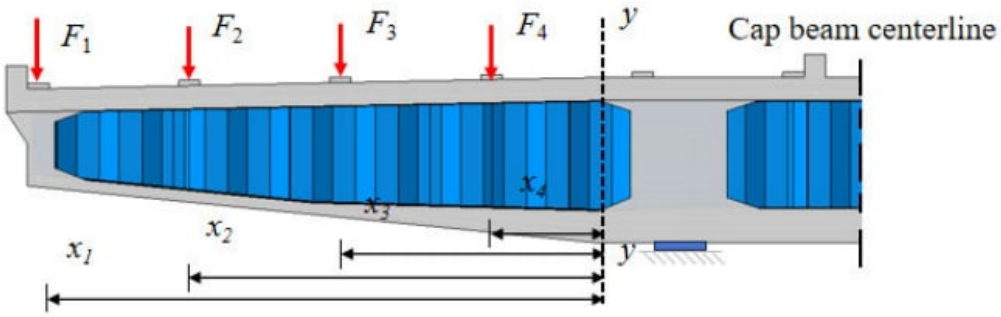

Figure 19. Schematic of external loads for the half CBC-CSW specimen.

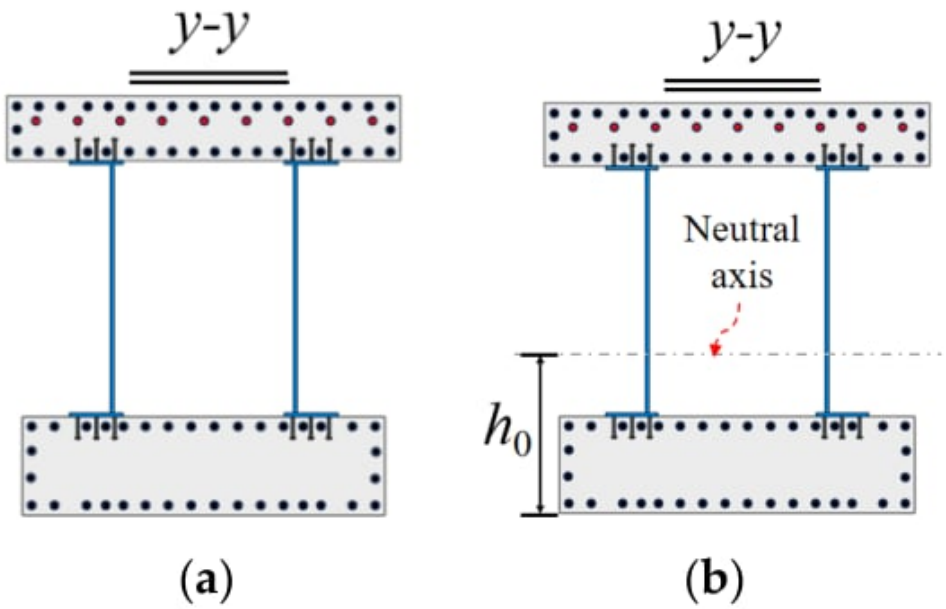

Figure 20. Schematic diagram of the cross-section: (**a**) schematic diagram of y-y sections; (**b**) neutral axis position of the cross-section.

The height of the concrete compression zone is calculate using Equation (9):

$$f_{sd1}A_{s1} + f_{pd}A_p + f_{tf.d}A_{tf} = \alpha_1\beta_1 f_{cd}bx + f_{sd2}A_{s2} + f_{bf.d}A_{bf} \quad (9)$$

where f_{sd1}, f_{pd} and $f_{tf.d}$ denote the design tensile strength of common steel rebars in the tension zone, prestressing tendons, and flange steel of corrugated steel webs, respectively (MPa); A_{s1}, A_p, A_{tf}, A_{s2} and A_{bf} represent the cross-sectional area of common steel rebars in the tension zone, prestressing tendons, upper flange of corrugated steel webs, common steel rebars in the compression zone, and lower flange of corrugated steel webs, respectively (mm^2); $f_{bf.d}$, f_{sd2} and f_{cd} are, respectively, defined as the design tensile strength of corrugated steel web flange steel, design tensile strength of common steel rebars in the compression zone, and design compressive strength of concrete in the compression zone, in MPa; b represents the width of the concrete bottom plate, in mm; x denotes the height of the concrete compression zone, in mm; α_1, β_1 are coefficients for the equivalent rectangular stress diagram of concrete.

Theoretical assumptions adopted in this study are as follows: (I) flexural behavior of normal sections complies with the quasi-plane section hypothesis; (II) tensile strength of concrete is neglected; (III) stress distribution across component sections remains uniform under ultimate flexural state; (IV) no relative slip occurs between concrete and steel reinforcement; (V) corrugated steel webs exhibit no flexural capacity.

When calculating the flexural capacity of CBC-CSW, the common steel rebars and prestressed steel bundles are assumed to attain their design tensile strength, while the compressed concrete is considered to reach its design compressive strength.

The bending moment capacity M_u of the CBC-CSW is calculated by establishing the moment equilibrium equation about the neutral axis.

$$M_u = M_{pu} + M_{su1} + M_{tf.u} + M_{bf.u} + M_{su2} + M_{cu} \quad (10)$$

where M_u, M_{pu}, M_{su1}, $M_{tf.u}$, $M_{bf.u}$, M_{su2} and M_{cu} are the flexural capacities provided by the CBC-CSW, prestressing tendons, tensile common steel rebars, upper flange of the corrugated steel web at the neutral axis, lower flange of the corrugated steel web at the neutral axis, compressive common steel rebars, and compressive concrete, respectively, in kN·m.

In Equation (10), the flexural capacity of each component is determined by the product of the strength design value, cross-sectional area, and distance from the neutral axis (Equation (10)). This formulation was then reformulated to derive Equation (11), yielding the flexural capacity formula for CBC-CSW.

$$\begin{aligned} M_u = f_{py}A_p|h_p - h_0| + f_{sd1}A_{s1}|h_{s1} - h_0| + f_{tf.y}A_{tf}|h_{tf} - h_0| + f_{bf.y}A_{bf}|h_{bf} - h_0| \\ + f_{sd2}A_{s2}|h_{s2} - h_0| + f_{cd}A_c|h_c - h_0| \end{aligned} \quad (11)$$

When the superimposed bending moment M_y induced by external loads at the y-y section exceeds the ultimate flexural capacity M_u, the ultimate flexural state of the corrugated steel web is attained. Figure 21 compares the theoretical calculations with FEM results. The maximum discrepancy is 9.56%, with all relative errors (δ) falling within 10% and primarily distributed between 5% and 7%. This confirms the high consistency between FEM and theoretical methods, demonstrating that the proposed flexural capacity calculation method-based on plane section assumption and bending mechanism-provides a reliable theoretical reference for studying the flexural behavior of CBC-CSW.

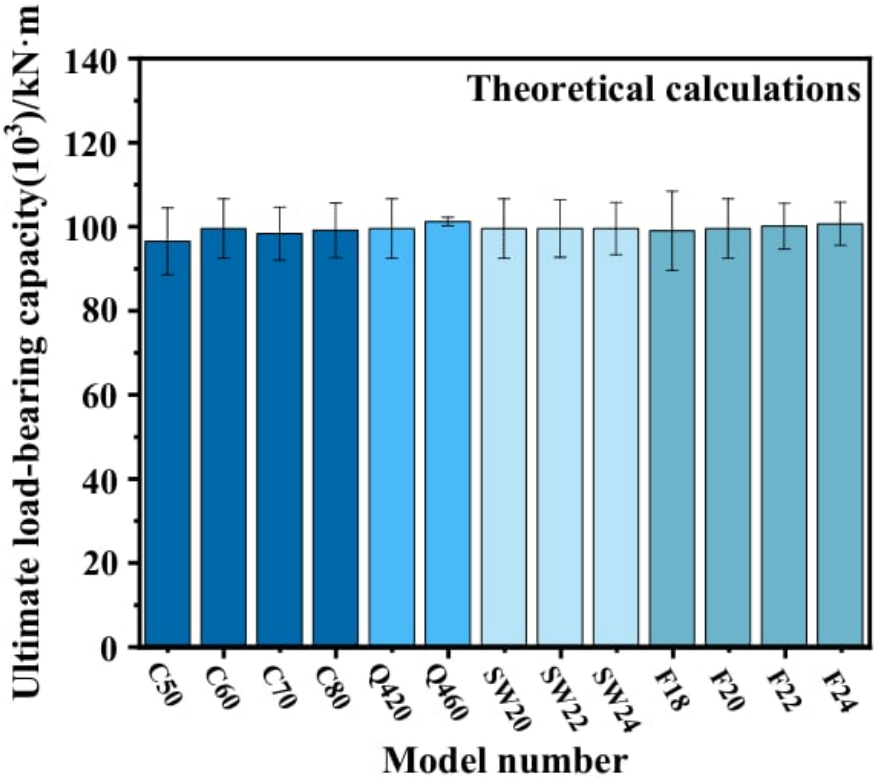

Figure 21. Comparative analysis diagram of FEM and theoretical calculation of flexural capacity.

6. Conclusions

This study investigated the flexural behavior of fully prefabricated large-cantilever CBC-CSW through full-scale testing, finite element analysis, and theoretical investigation, proposing a calculation method for their flexural capacity. The main conclusions are as follows:

(1) CBC-CSW adopts corrugated steel webs to replace conventional concrete webs, achieving a self-weight reduction of more than 50%, which facilitates factory prefabrication and on-site hoisting construction. Full-scale non-destructive static tests were performed on two CBC-CSW specimens using a self-designed reaction-force loading setup. The test results indicate that under the characteristic combination load for the serviceability limit state, the CBC-CSW remains in the elastic working stage. The concrete top plate of the bent cap is subjected to tension, while the concrete bottom plate is under compression. The longitudinal stress within the corrugated steel webs maintains a relatively low level, and the strain distribution along the height of the bent-cap section complies with the plane-section assumption.

(2) Based on the full-scale static loading test results, a validated refined FEM of CBC-CSW was established to analyze the ultimate bearing capacity of the structure. The mechanical response of CBC-CSW under bending was divided into three distinct phases: the elastic stage, yield stage, and failure stage. The cracking load was found to be 23,146.4 kN, where initial tensile cracks appeared at the top plate of the cantilever-root section. At a load of 32,170.3 kN, severe crack concentration was observed on the top-plate surface. As the load further increased to 34,275.7 kN, the CBC-CSW experienced flexural failure.

(3) Finite-element parametric analysis reveals that when the concrete strength increases from 50 MPa to 80 MPa, the flexural capacity of the bent cap increases by merely 4.56%, and the component still fails in flexure. When the steel plate strength rises from 355 MPa to 490 MPa and the corrugated steel web thickness increases from 18 mm to 24 mm, the bearing capacity of the bent cap increases by 57.25% and 17.35%, respectively. Such considerable capacity improvement essentially stems from the transition of failure mode from shear failure to flexural failure. The steel flange can improve the flexural performance of the bent cap; when the thickness of the steel flange increases from 18 mm to 24 mm, the bearing capacity rises by 6.69%, and flexural failure is still observed for the component.

(4) Based on the flexural mechanism of CBC-CSW and the plane-section assumption, a flexural-capacity calculation method is proposed. The maximum deviation between theoretical predictions and finite-element results reaches 9.56%, and all relative errors δ are less than 10%, mostly falling within the range of 5–7%. These findings verify the favorable accuracy of the proposed method, which can provide support for the flexural-capacity evaluation and structural optimization design of CBC-CSW.

(5) This study mainly focuses on the flexural performance of CBC-CSW under static service-level loads. Further research should be carried out on its shear behavior, fatigue performance under repeated vehicle loads, and mechanical characteristics of key connections, so as to support its popularization and practical application in bridge engineering.

Author Contributions: Conceptualization, W.L. and L.H.; methodology, W.L., P.H. and Z.C.; software, Z.C.; validation, P.H. and F.L.; formal analysis, Z.C. and P.H.; investigation, Z.C. and F.L.; resources, W.L. and L.H.; data curation, Z.C.; writing—original draft preparation, Z.C.; writing—review and editing, W.L., Z.C., P.H. and F.L.; visualization, Z.C. and F.L.; supervision, L.H.; project administration, F.L. and P.H.; funding acquisition, F.L. and P.H. All authors have read and agreed to the published version of the manuscript.

Funding: This research was funded by the Henan Key Research and Development Program (Grant Number 231111241500); the Zhongyuan Science and Technology Innovation Leading Talent Program (Grant Number 244200510019); the Natural Science Foundation of Henan Province (Grant Number 242300420434); and the Key Research Project of Higher Education Institutions of Henan Province (Grant Number 26A560006).

Data Availability Statement: For data from the study, please contact the corresponding author at 18539836692@163.com.

Conflicts of Interest: Author Panfeng Hou was employed by Henan Transport Investment Group Co., Ltd., Author Feiran Li was employed by Henan Zhonggong Design & Research Group Co., Ltd., Author Lu Huang was employed by China Construction Seventh Engineering Division Corp., Ltd. The remaining authors declare that the research was conducted in the absence of any commercial or financial relationships that could be construed as a potential conflict of interest.

References

1. Zhang, Z.; Guo, F.; Gao, J.; Deng, E.; Kong, J.; Zhang, L. Seismic performance of an innovative prefabricated bridge pier using rapid hardening ultra-high performance concrete. *Structures* **2025**, *74*, 108558. [CrossRef]
2. Shoushtari, E.; Saiidi, M.S.; Itani, A.; Moustafa, M.A. Seismic performance of a two-span steel girder bridge with ABC connections. *Eng. Struct.* **2021**, *241*, 112502. [CrossRef]
3. DO, T.A.; Chen, H.; Leon, G.; Nguyen, T. A combined finite difference and finite element model for temperature and stress predictions of cast-in-place cap beam on precast columns. *Constr. Build. Mater.* **2019**, *217*, 172–184. [CrossRef]
4. Shao, X.; Zeng, H.; Cao, J. Flexural behavior of fully prefabricated large-cantilevered high strength steel-UHPC composite bent caps. *J. Constr. Steel Res.* **2023**, *204*, 107856. [CrossRef]
5. Chen, K.; Lin, Y.; Wang, Z.; Zheng, Y.; Wang, W. Shear and tensile bonding performance of prefabricated UHPC and cast-in-place NC interface in composite girder bridges. *Constr. Build. Mater.* **2025**, *462*, 139952. [CrossRef]
6. Jiang, J.; Wang, H.; Zhou, Z.; Liang, H.; Zhang, Z.; He, Z.; Zou, Y. Flexural behavior of prefabricated steel-UHPC composite beams with hollow UHPC bridge deck. *J. Constr. Steel Res.* **2025**, *226*, 109267. [CrossRef]
7. Liu, H.; Wang, H.; Zhang, Y.; Liu, X. Shear resistance of UHPC connection for prefabricated reinforced concrete slabs with shear grooves and dowel rebars. *Constr. Build. Mater.* **2024**, *454*, 139153. [CrossRef]
8. Liu, C.; Pan, L.; Liu, H.; Tong, H.; Yang, Y.; Chen, W. Experimental and numerical investigation on mechanical properties of grouted-sleeve splices. *Constr. Build. Mater.* **2020**, *260*, 120441. [CrossRef]
9. Yang, H.; Yu, P.; Zheng, Y. Experimental evaluation of a novel demountable shear connection system in prefabricated steel-concrete composite beams. *Constr. Build. Mater.* **2025**, *470*, 140624. [CrossRef]
10. Ye, M.; Li, L.; Hu, F.; Shao, X.; Tang, J. Flexural Behavior of a Fully Prefabricated Lightweight UHPC Bent Cap. *J. Bridge Eng.* **2020**, *25*, 04020085. [CrossRef]
11. Jiang, R.; Au, F.; Xiao, Y. Prestressed Concrete Girder Bridges with Corrugated Steel Webs: Review. *J. Struct. Eng.* **2015**, *141*, 04014108. [CrossRef]
12. Easley, J. Buckling Formulas for Corrugated Metal Shear Diaphragms. *J. Struct. Div.* **1975**, *101*, 1403–1417. [CrossRef]
13. Yi, J.; Gil, H.; Youm, K.; Lee, H. Interactive shear buckling behavior of trapezoidally corrugated steel webs. *Eng. Struct.* **2008**, *30*, 1659–1666. [CrossRef]
14. Oh, J.; Lee, D.; Kim, K. Accordion effect of prestressed steel beams with corrugated webs. *Thin-Walled Struct.* **2012**, *57*, 49–61. [CrossRef]
15. Moon, J.; Yi, J.; Choi, B.H.; Lee, H.-E. Shear strength and design of trapezoidally corrugated steel webs. *J. Constr. Steel Res.* **2009**, *65*, 1198–1205. [CrossRef]
16. Moon, J.; Yi, J.; Choi, B.-H.; Lee, H.-E. Shear Design of Trapezoidally Corrugated Steel Webs. *J. Korean Soc. Civ. Eng. A* **2008**, *28*, 497–505.
17. Deng, W.; Zhou, M.; Hassanein, M.F.; Zhang, J.; Liu, D.; An, L. Growth of prestressed concrete bridges with corrugated steel webs in China. *Proc. Inst. Civ. Eng.-Civ. Eng.* **2018**, *171*, 77–84. [CrossRef]
18. He, J.; Wang, S.; Liu, Y.; Dai, L.; Lyu, Z.; Li, C.; Xin, H.; Tan, C. The development of composite bridges with corrugated steel webs in China. *Proc. Inst. Civ. Eng.-Bridge Eng.* **2020**, *174*, 28–44. [CrossRef]
19. He, J.; Liu, Y.; Chen, A.; Yoda, T. Mechanical behavior and analysis of composite bridges with corrugated steel webs: State-of-the-art. *Int. J. Steel Struct.* **2012**, *12*, 321–338. [CrossRef]
20. Deng, H.; Shao, Y.; Hassanein, M. Experimental shear testing of small-scale corrugated web girders used in conventional buildings. *J. Constr. Steel Res.* **2022**, *189*, 107086. [CrossRef]

21. Karakoti, A.; Kar, V. Deformation characteristics of sinusoidally-corrugated laminated composite panel—A higher-order finite element approach. *Compos. Struct.* **2019**, *216*, 151–158. [CrossRef]
22. Wang, S.; He, J.; Liu, Y.; Li, C.; Xin, H. Shear capacity of a novel joint between corrugated steel web and concrete lower slab. *Constr. Build. Mater.* **2018**, *163*, 360–375. [CrossRef]
23. Feng, S.; He, J.; Zhu, Y.; Luo, C.; Xin, H.; Lin, W.; Vasdravellis, G. A replaceable corrugated web shear link for seismic resilience of double-column bridge bent: Experimental, numerical, and theoretical study. *Constr. Build. Mater.* **2025**, *491*, 142829. [CrossRef]
24. Zhao, G.; Liu, J.; Meng, S.; Liu, C.; Wang, Q. Performance of corrugated steel plate flange joint under combined compression and Bending: Experimental and numerical investigations. *Constr. Build. Mater.* **2023**, *389*, 131798. [CrossRef]
25. Chen, Y.; Dong, J.; Xu, T.; Xiao, Y.; Jiang, R.; Nie, X. The shear-lag effect of composite box girder bridges with corrugated steel webs and trusses. *Eng. Struct.* **2019**, *181*, 617–628. [CrossRef]
26. Hassanein, M.; Kharoob, O. Shear buckling behavior of tapered bridge girders with steel corrugated webs. *Eng. Struct.* **2014**, *74*, 157–169. [CrossRef]
27. Elamary, A.; Ahmed, M.; Mohmoud, A. Flexural behaviour and capacity of reinforced concrete-steel composite beams with corrugated web and top steel flange. *Eng. Struct.* **2017**, *135*, 136–148. [CrossRef]
28. Bi, Z.; Yang, G. Steel-concrete composite girders with corrugated steel webs: Accordion effects. *J. Constr. Steel Res.* **2025**, *224*, 109114. [CrossRef]
29. Metwally, A.; Loov, R. Corrugated steel webs for prestressed concrete girders. *Mater. Struct.* **2003**, *36*, 127–134. [CrossRef]
30. Oliveira, J.; Calenzani, A.; Fakury, R.H.; Ferreira, W.G. Elastic critical moment of continuous composite beams with a sinusoidal-web steel profile for lateral-torsional buckling. *Eng. Struct.* **2016**, *113*, 121–132. [CrossRef]
31. He, J.; Liu, Y.; Chen, A.; Wang, D.; Yoda, T. Bending behavior of concrete-encased composite I-girder with corrugated steel web. *Thin-Walled Struct.* **2014**, *74*, 70–84. [CrossRef]
32. Chen, Y.; Dong, J.; Xu, T. Composite box girder with corrugated steel webs and trusses—A new type of bridge structure. *Eng. Struct.* **2018**, *166*, 354–362. [CrossRef]
33. He, J.; Liu, Y.; Xu, X.; Li, L. Loading capacity evaluation of composite box girder with corrugated webs and steel tube slab. *Struct. Eng. Mech.* **2014**, *50*, 501–524. [CrossRef]
34. Pekgokoz, R.K.; Izol, G.; Avcil, F.; Gurel, M.A. Experimental and numerical investigation of the tendon layout effect on flexural capacity in post-tensioning beams. *Teh. Vjesn.* **2024**, *31*, 1553–1560. [CrossRef]
35. Elgaaly, M.; Seshadri, A.; Hamilton, R. Bending Strength of Steel Beams with Corrugated Webs. *J. Struct. Eng.* **1997**, *123*, 772–782. [CrossRef]
36. *GB/T50010-2010*; Design Standard for Concrete Structures. China Architecture & Building Press: Beijing, China, 2011.
37. Zheng, S.; Liu, Y.; Yoda, T.; Lin, W. Parametric study on shear capacity of circular-hole and long-hole perfobond shear connector. *J. Constr. Steel Res.* **2016**, *117*, 64–80. [CrossRef]
38. Blakeley, R.; Park, R. Ductility of prestressed concrete members. *Bull. N. Z. Soc. Earthq. Eng.* **1971**, *4*, 145–170. [CrossRef]
39. Hu, H.; Wang, J.; Yan, X.; Ge, J.; Zhang, D. Experimental research and numerical analysis on mechanical behavior of lightweight-design precast bent caps with large cantilevers. *Structures* **2022**, *40*, 536–554. [CrossRef]

Disclaimer/Publisher's Note: The statements, opinions and data contained in all publications are solely those of the individual author(s) and contributor(s) and not of MDPI and/or the editor(s). MDPI and/or the editor(s) disclaim responsibility for any injury to people or property resulting from any ideas, methods, instructions or products referred to in the content.